Journal of Thermal Analysis and Calorimetry (2020) 140:2185–2201
https://doi.org/10.1007/s10973-019-08962-7

Aqueous sol–gel synthesis, thermoanalytical study and luminescent properties of $M_{0.05}Eu_{0.05}Ca_{0.9}MoO_4$ (M=Li, Na, K, Rb, Cs) nanocrystallites

Giedrė Gaidamavičienė[1] · Gytautas Janulevičius[1] · Eglė Venslauskaitė[1] · Artūras Žalga[1]

Received: 18 June 2019 / Accepted: 25 October 2019 / Published online: 6 November 2019

Abstract
Nano-sized $M_{0.05}Eu_{0.05}Ca_{0.9}MoO_4$ (M=Li, Na, K, Rb, Cs) ceramics have been successfully synthesized by an aqueous sol–gel synthesis method using a tartaric acid as a ligand. In order to reveal the influence of the peculiarities of the nature of dopants effect into the crystallization of $CaMoO_4$ double oxide, the thermal analysis of the as-prepared gels was performed. In addition, infrared spectroscopy was used in order to identify the functional groups from the characteristic stretching vibrations in the M–Eu–Ca–Mo–O tartrate gel precursors. Besides, to confirm the dynamics of growing crystallites in the final ceramics and to reveal the morphological changes on the surface, the x-ray diffraction and scanning electron microscopy were applied. Finally, photoluminescence measurements were used to estimate the optical properties of europium oxide as a dopant in the samples according to the nature of alkali metal. Therefore, according to the obtained results, it was estimated that luminescence intensity of Eu^{3+} ions is mainly affected by the chemical reaction, which takes place at about 973 K of temperature. This effect was partly confirmed from the results of the thermal decomposition of M–Eu–Ca–Mo–O tartrate gel precursors with an endothermic behaviour in the DSC curve, which indicates the crystallization mechanism of the $CaMoO_4$ double oxide.

Keywords Sol–gel synthesis · Thermal analysis · X-ray diffraction · Rietveld refinement · Optical properties

Introduction

$CaMoO_4$ is a well-known and important material. For its unique chemical and optoelectrical properties, it has been used in various fields as a luminescent [1], optical fibre [2], magnetic [3] and solid-state laser [4] material. Additionally, it can be used in humidity sensors [5], photocatalysts [6], scintillators [7] and cryogenic detectors [8]. Predominantly, $CaMoO_4$ has scheelite crystal structure [9] responsible for luminescence in blue and green parts of the spectrum [10], when excited with UV rays in 250–310 nm wavelength interval [11]. Calcium molybdate is also characterized by its strong physical and chemical resistances, which make it the preferred over its predecessors like $Y_2O_2S:Eu^{3+}$, $YVO_4:Eu^{3+}$, $Y_2SiO_5:Tb^{3+}$ or $Gd_2O_2S:Tb^{3+}$ [12]. In this structure, the Mo atoms are bonded to four oxygen, forming the [13] clusters [14], which can absorb ultraviolet region with high absorption cross section [15]. Charge transfer between can be observed between [13] cluster and dopant ion [16], thus making it possible to achieve luminescence in different parts of the spectrum by doping $CaMoO_4$ with rare-earth elements (RE). This peculiarity allows this material to be used as a matrix incorporated or saturated with dopant elements. By doping calcium molybdate with europium (III) ions (Eu^{3+}), strong red luminescence is achieved [17], while doping with terbium (III) ions (Tb^{3+})—strong green luminescence [18, 19]. It was observed that doping $CaMoO_4$ with two or more ions: rare-earth element (RE^{3+}) and charge-compensating element, for example Bi^{3+} [20] or alkali metal (Li^+, Na^+, K^+), luminescence intensity, is significantly improved without increasing RE^{3+} ion amount [21]. However, previously reported studies utilize inefficient or complex methods of synthesis, such as solid state or hydrothermal. Additionally, those methods require high annealing temperatures above or at 1173 K.

In recent years, microstructure and surface morphology have been proven to be essential part for achieving

✉ Artūras Žalga
arturas.zalga@chf.vu.lt

[1] Department of Applied Chemistry, Institute of Chemistry, Faculty of Chemistry and Geosciences, Vilnius University, Naugarduko Str. 24, 03225 Vilnius, Lithuania

characterizing desired material properties [22]. Therefore, it is crucial to adequately choose a method and conditions for the synthesis of the desired material. There are several published methods, among which are: pulse laser ablation (PLA) [23], mixed oxide [24], molten salt [25], solid state [26], hydrothermal and its variations [13, 27, 28], Czochralski [29] and precipitation [30], but generally, scheelite-type phosphors are synthesized by conventional solid-state reaction method [31]. This approach usually requires annealing at high temperatures for several hours and subsequent grinding. This crushing process changes the phosphor surfaces, resulting in the loss of emission intensity. Therefore, demand for alternative synthesis methods such as hydrothermal method or sol–gel process arise, as it was also shown that phosphors prepared via an wet chemical routes have higher uniformity in particle-size distribution with high crystallinity and exhibit higher photoluminescence intensity than those prepared by the solid-state reaction [32]. Therefore, sol–gel is an important method for its simplicity, repeatability, mild synthesis conditions, potential industrial application and desirable achieved product morphology.

Moreover, we provide a simple aqueous route for synthesizing high-purity scheelite $CaMoO_4$ phase substituted with RE element and a charge-compensating alkali ion. To our knowledge, such scale research was not published yet, as most of the published material presents solid-state or hydrothermal synthesis, and none of it compares the effect of all the substituted alkali ions (Li, Na, K, Rb, Cs). Additionally, thermal characterization of these materials is very scarce. While previous materials used Eu(III) ion hosts have been reported to have poor thermal stability [33], similar structures, such as $Ho^{3+}/Tm^{3+}/Yb^{3+}$-codoped $CaWO_4$, have been reported to have very high thermal stability, with only phase transition/organic impurity decomposition below 773 K after which the mass remained constant [34]. On the other hand, it gives this work an extra novelty and relevance, because of this synthesis technique that is based on the use of tartaric acid as a ligand during the sol–gel processing, which is powerful enough to prepare pure calcium molybdate with stabile crystal structure, uniform surface morphology and identical properties [35, 36]. Besides, our proposed synthesis procedure does not have any side effects to the final ceramic product and there are no typical undesirable consequences for the environment because of uses of tartaric acid that is found in food industry. According to that, it is obvious that this research enables to estimate the influence of the nature of alkali metal to the luminescent properties of Eu^{3+} ion in the host of $CaMoO_4$.

Materials and methods

The samples of $M_{0.05}Eu_{0.05}$ $Ca_{0.9}MoO_4$ (M=Li, Na, K, Rb, Cs) were prepared by the tartaric acid-assisted synthesis (TAS) approach during the mixing stage of the initial salts employing an tartaric acid as a chelating agent that interacts as a ligand at the molecular level with the reaction mixture during the both dissolution in water and sol–gel formation.

Lithium (I) nitrate ($LiNO_3$, 99% Alfa Aesar), sodium (I) nitrate ($NaNO_3$ 99,5% Alfa Aesar), potassium (I) nitrate (KNO_3, 99,5% Alfa Aesar), rubidium (I) nitrate ($RbNO_3$ 99.9% Alfa Aesar), caesium (I) nitrate ($CsNO_3$, 99,8% Alfa Aesar), europium (III) oxide (Eu_2O_3, 99.99% Alfa Aesar), calcium (II) nitrate tetrahydrate ($Ca(NO_3)_2{\cdot}4H_2O$ 99% Alfa Aesar) and molybdenum (VI) oxide (MoO_3, 99.95% Alfa Aesar) were used as starting materials and weighed according to the desired stoichiometric ratio (Table 1).

Nitric acid (HNO_3 66% Reachem), distilled water and concentrated ammonia solution ($NH_3{\cdot}H_2O$ 25% Penta) were used as solvents and reagents to regulate the pH of the solutions. Tartaric acid (L–(+)–Tartaric acid ($C_4H_6O_6$) (TA) ≥ 99.5% Sigma-Aldrich) was applied for escalation

Table 1 Stoichiometric amount, molecular weight, melting and boiling points for the corresponding salts, which were used during the sol–gel synthesis procedure

Chemical formula	Amount/mol	Molecular weight[a]/g mol^{-1}	Melting point[a]/K	Solubility[a] in water/g L^{-1}
$LiNO_3$	0.05	68.946	528	522 at 293 K
$NaNO_3$	0.05	84.995	581	912 at 298 K
KNO_3	0.05	101.103	607	242 at 293 K
$RbNO_3$	0.05	147.473	581	650 at 298 K
$CsNO_3$	0.05	194.91	687	270 at 298 K
Eu_2O_3	0.05	351.926	2623	Negligible
$Ca(NO_3)_2{\cdot}4H_2O$	0.9	236.15	320	1290 at 293 K
MoO_3	1	143.95	1075	0.490 at 301 K
HNO_3	0.4431	63.0129	231	Miscible
$NH_3{\cdot}H_2O$	0.01336	17.031	195.4	310 at 298 K
$C_4H_6O_6$	4	150.087	446	575 at 293 K

[a]Information about the physical properties of reagents was gathered from the supplier

of solubility via coordination of starting compounds in the reaction mixture, especially, during the pH changes and evaporation before sol–gel formation. The synthesis scheme for the preparation of M–Eu–Ca–Mo–O tartrate gel precursors is shown in Fig. 1.

At first, MoO_3 was dissolved in a solution that consisted of 25 mL of distilled water and 1 mL of concentrated ammonia by stirring at 355–360 K of temperature. Then, after continuous stirring at approximately 355–360 K as long as the excess of ammonia had been evaporated, the tartaric acid was added to the reaction mixture. The amount of tartaric acid is directly related to the concentration of molybdenum oxide according to their molar ratio of Mo/TA = 0.25. After the dissolution of tartaric acid in the reaction mixture, the required amount of alkali metal nitrate was added. Then, under the continuous stirring and heating, the europium (III) oxide and concentrated nitric acid were poured to the beaker. A clear yellowish solution was obtained and subsequently concentrated by slowly vaporizing the reaction mixture at 360 K.

In the following stage, a yellow transparent sol was formed after nearly 95% of the water had been evaporated. After drying the sol precursor in an oven at 393 K, the fine-grained light brown gel powders were obtained. The well-dried gel powders were used for the thermal analysis in order to estimate their decomposition mechanism. Meanwhile, the residue of gel precursors was additionally heat-treated at the temperatures of 623 K, 673 K, 773 K, 873 K, 973 K, 1073 K, 1223 K and 1273 K for 5 h in the air.

Thermal measurements were taken with TG−DSC, STA 6000 PerkinElmer instrument using a sample weight of about 10 mg and a heating rate of 20° min^{-1} under the continuous air flow (20 cm^3 min^{-1}) at ambient pressure from room temperature to 1223 K. The Fourier transform infrared (FT-IR) spectra for the M–Eu–Ca–Mo–O tartrate gel precursors were recorded with a PerkinElmer Frontier FT-IR spectrometer. The corresponding gel precursors heat-treated at different temperatures, and the residual powders that were left after the thermal treatment were additionally investigated by x-ray diffraction (XRD) analysis. The XRD patterns were recorded in air at room temperature with a powder x-ray diffract meter Rigaku MiniFlex II using CuKα_1 radiation. The patterns were recorded at the standard rate of 1.5 2θ/min^{-1}. In addition, the Rietveld refinement of the obtained XRD patterns was performed using X'Pert High-Score Plus software. The scanning electron microscope (SEM) Hitachi SU-70 was used to study the surface morphology and microstructure of the obtained ceramic samples. Finally, the measurements of photoluminescence (PL) and photoluminescence excitation (PLE) spectra were taken by using a PerkinElmer LS-55 spectrometer.

Results and discussion

Thermal analysis

The TG/DTG/DSC measurements of the M–Eu–Ca−Mo–O tartrate (M=Li, Na, K, Rb, and Cs) gel precursors, which were taken up to 1223 K at a heating rate of 20° min^{-1} in flowing air (20 cm^3 min^{-1}) at ambient pressure with a sample mass of about 10 mg are shown in Fig. 2, respectively.

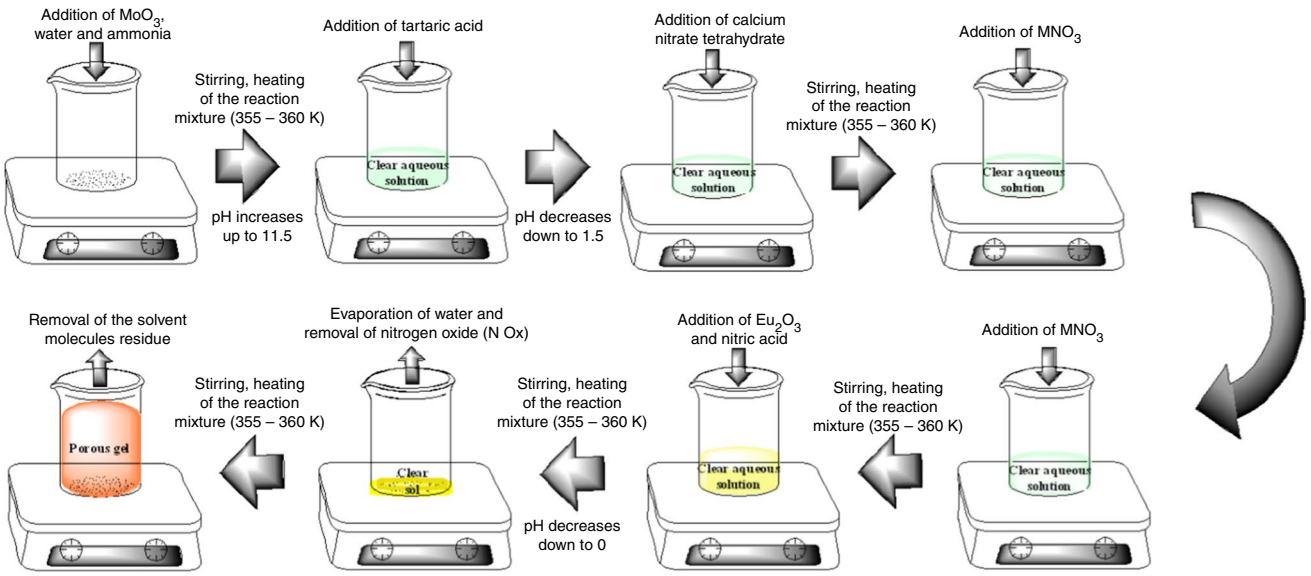

Fig. 1 Synthesis scheme of the sol–gel preparation for the M–Eu–Ca–Mo–O tartrate gel precursors and $M_{0.05}Eu_{0.05}Ca_{0.9}MoO_4$ (M=Li, Na, K, Rb, Cs) ceramics

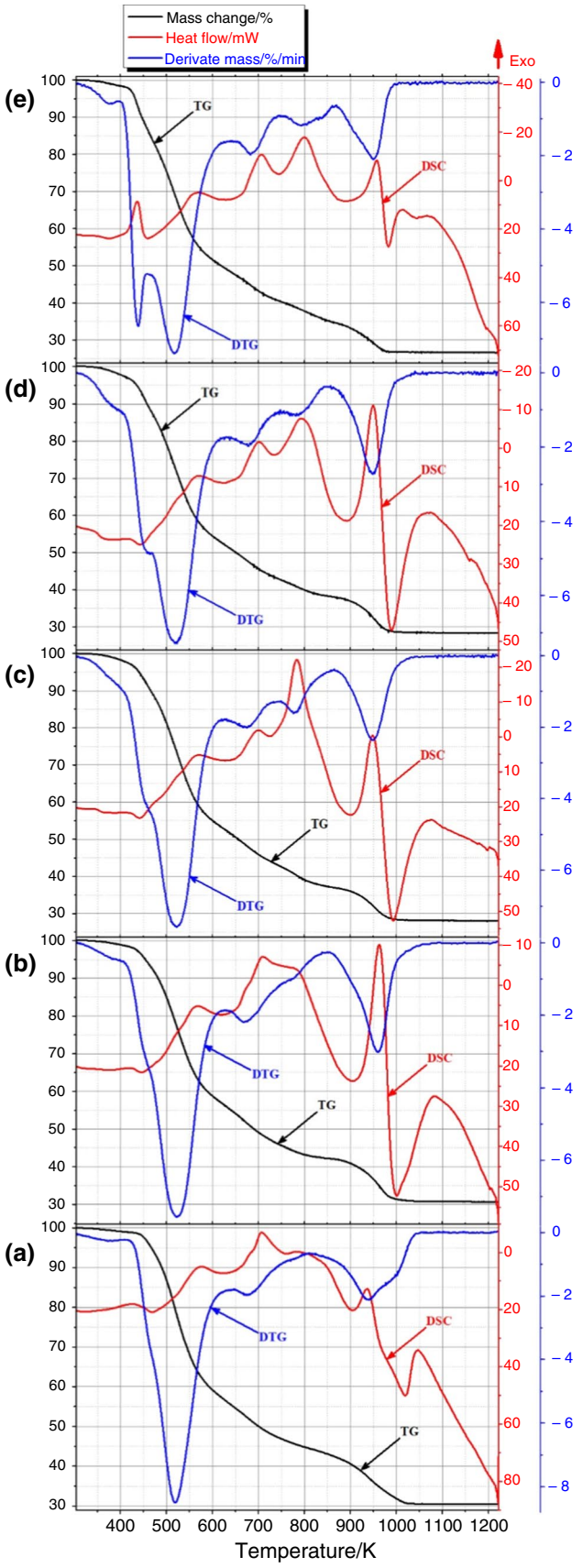

Fig. 2 Combined TG–DTG–DSC curves of the Li–Eu–Ca–Mo–O tartrate gel precursor for $Li_{0.05}Eu_{0.05}Ca_{0.9}MoO_4$ (**a**), $Na_{0.05}Eu_{0.05}Ca_{0.9}MoO_4$ (**b**), $K_{0.05}Eu_{0.05}Ca_{0.9}MoO_4$ (**c**), $Rb_{0.05}Eu_{0.05}Ca_{0.9}MoO_4$ (**d**) and $Cs_{0.05}Eu_{0.05}Ca_{0.9}MoO_4$ (**e**) ceramics

Tables 2–6 show data, which were deducted from Fig. 2 and supplements quantitatively the general view of thermal decomposition processes in M–Eu–Ca–Mo–O tartrate gel precursors.

In addition, it is also important to note that in the frame of this study a new investigation approach to the analysis of the thermal processes was applied during which it is possible to reveal and to calculate the overlapping chemical and physical changes. In this case, the nature of alkali metal plays a very important role, taking into account that all synthesis procedures were made in similar manner, and the way of the thermal decomposition of initial gels was not identical. These discrepancies allow us to estimate the influence of both the initial composition to the crystallization for the final ceramic materials and thermal decomposition of intermediate organic parts from the gel precursors. Especially, an important role goes to the exothermic effect in the DSC curve between 400 and 450 K of temperature, which thermal behaviour tends to increase by changing the nature of alkali metal in the sample. This exothermic effect was identified from the slope of DTG curves, which gradually converts into the peak by changing the nature of alkali metal in the initial composition. In our previous report, [37] we suggested a stage between the temperature of 421 K and 493 K assign to the thermal decomposition of tartaric-acids dimer ($C_8H_8O_{10}$) into carbon monoxide (CO), carbon dioxide (CO_2) and two acetic acid (CH_3COOH) molecules. Meanwhile, by investigating this case, it is clear that the decomposition effect of tartaric-acids dimer is not very well pronounced and this process is closely related to the evaporation and removal of volatile components from the M–Eu–Ca–Mo–O tartrate gel. Besides, an enhanced ionic character of the alkali metal reduces the coordination of unreacted tartaric acid molecules, for that reason their decomposition into the carbon oxides occurs at much lower temperature than was expected. Nevertheless, the decomposition of unreacted tartaric acid occurs up to 568 K in all cases with the mass loss of about 36–43%. The mass of the gel precursors during this decomposition stage, in the range of temperature from 300 K to 568 K, decreases by 36–37%, and this is typical for $Li_{0.05}Eu_{0.05}$ $Ca_{0.9}MoO_4$ and $Na_{0.05}Eu_{0.05}$ $Ca_{0.9}MoO_4$ initial composition compounds. Meanwhile, the mass change for K–Eu–Ca–Mo–O and Rb–Eu–Ca–Mo–O tartrate gel precursors increases to 40.261% and 41.176%, respectively, indicating enhanced ionic character of corresponding alkali metals. Moreover, the thermal behaviour of DSC curve clearly shows several heat

Table 2 Thermoanalytical data of the Li–Eu–Ca−Mo–O tartrate gel precursor for $Li_{0.05}Eu_{0.05}Ca_{0.9}MoO_4$ ceramic

Stage No.	Range of temperature/K	Mass			Heat			
		Change/%	Onset/K	Residual/%	Flow/mJ	Onset/K	End/K	Enthalpy/J g^{-1}
I	**299.15–567.71**	**36.340**	–	**63.660**	**|3417.3295|**	–	–	**|338.6415|**
	299.15–423.68	1.179	300.20	98.821	365.822	301.55	404.32	36.2513
	335.15–472.24	5.800	447.99	94.068	–524.763	383.35	464.31	–52.0016
	423.68–**567.71**	34.997	545.60	**63.660**	1757.492	435.12	555.62	174.1593
	476.16–651.87	38.937	553.25	54.645	–1538.505	516.39	619.13	–152.4586
II	**567.71–837.64**	**20.243**	–	**43.417**	**|5595.698|**	–	–	**|554.50745|**
	567.71–706.09	14.506	569.37	49.554	1987.493	578.00	702.20	196.9512
	651.87–745.76	7.222	690.09	47.226	–1263.800	680.80	739.16	–125.2367
	706.09–**837.68**	6.021	757.92	**43.417**	512.477	715.29	826.02	50.7841
	752.76–899.13	6.165	872.98	40.680	–2125.351	–	884.56	–210.6123
III–IV	**837.64–1047.87**	**12.858**	–	**30.559**	**|11,965.847|**			**|1185.75945|**
	837.64–938.93	6.281	901.72	37.235	1630.386	853.23	933.35	161.5636
	899.13–1016.58	9.677	964.84	30.940	–2001.290	909.78	966.97	–198.3185
	938.93–**1047.87**	6.673	975.40	**30.559**	4262.548	943.70	1039.35	422.3986
	1016.58–1214.46	0.408	1016.65	30.559	–6017.895	1023.88	1209.91	–596.3452
V	**1047.87–1219.40**	**0**	–	**30.559**	**|3008.9475|**	–	–	**|298.1726|**

Bold values denote important points which summarize and relate obtained results in each stage of the thermal decomposition of the gel precursors

Table 3 Thermoanalytical data of the Na–Eu–Ca−Mo–O tartrate gel precursor for $Na_{0.05}Eu_{0.05}Ca_{0.9}MoO_4$ ceramic

Stage No.	Range of temperature/K	Mass			Heat			
		Change/%	Onset/K	Residual/%	Flow/mJ	Onset/K	End/K	Enthalpy/J g^{-1}
I	**298.54–566.54**	**36.662**	–	**63.338**	**|1262.226|**	–	–	**|123.58265|**
	298.54–419.54	1.719	300.50	98.281	226.062	302.31	406.41	22.1304
	366.02–447.46	3.612	433.19	95.978	–93.623	388.65	439.89	–9.1653
	422.23–519.29	19.718	487.93	78.200	684.940	–	517.40	67.0524
	457.87–538.74	22.913	492.14	71.294	–28.362	505.18	537.85	–2.7765
	519.29–**566.54**	14.981	532.95	**63.338**	16.569	–	549.07	1.6220
	538.74–634.95	15.954	541.68	55.573	–425.340	539.29	604.06	–41.6387
II	**566.54–791.67**	**19.756**	–	**43.582**	**|2340.106|**	–	–	**|229.0853|**
	566.54–671.01	11.361	676.73	51.753	854.829	572.39	669.81	83.6837
	634.95–685.80	4.960	668.36	50.284	–26.063	662.24	672.43	–2.5515
	671.01–705.97	3.620	671.92	48.668	32.084	–	694.64	3.1409
	685.80–733.87	3.863	697.88	46.464	–286.833	686.37	726.13	–28.0796
	705.97–**791.67**	4.947	733.62	**43.582**	71.851	720.17	774.70	7.0338
	733.87–909.17	6.279	734.87	40.293	–1711.552	741.97	849.23	–167.5529
III–IV	**791.67–1081.89**	**12.944**	–	**30.638**	**|29,800.0545|**	–	–	**|2917.27405|**
	791.67–964.67	8.895	960.52	34.637	9905.070	795.43	958.53	969.6593
	909.17–997.02	8.959	961.69	31.491	–5755.782	927.70	988.22	–563.4637
	964.67–**1081.89**	3.878	971.69	**30.638**	9153.367	970.79	1067.04	896.0614
	997.02–1.204.68	0.769	1004.57	30.670	–8260.119	1020.85	808.74	–808.6264
V	**1081.89–1223**	**0.047**		**30.591**	**|4130.0595|**	–	–	**|404.3132|**

Bold values denote important points which summarize and relate obtained results in each stage of the thermal decomposition of the gel precursors

Table 4 Thermoanalytical data of the K−Eu–Ca−Mo–O tartrate gel precursor for $K_{0.05}Eu_{0.05}Ca_{0.9}MoO_4$ ceramic

Stage No.	Range of temperature/K	Mass			Heat			
		Change/%	Onset/K	Residual/%	Flow/mJ	Onset/K	End/K	Enthalpy/J g^{-1}
I	**300–566.72**	**40.268**	–	**59.732**	**|833.988|**	–	–	**|82.66305|**
	300–363.15	0.257	300.45	99.743	41.258	302.29	–	4.0894
	320–363	0.412	358.34	99.588	–37.501	–	357.54	–3.7170
	363.15–417	2.357	407.07	97.485	75.906	349.83	–	7.5237
	363.14–443.15	4.557	426.84	94.967	–115.882	386.74	437.04	–11.4859
	417.15–470.15	7.755	442.80	89.448	192.597	423.94	467.02	19.0898
	443.15–496.15	11.268	448.49	83.068	–18.070	455.73	–	–1.7911
	470.15–520.15	14.713	491.53	74.26	54.380	–	514.74	5.3900
	496.15–**566.72**	13.003	508.91	**59.732**	–29.444	–	498.42	–2.9184
	566.72–643.15	17.560	563.50	51.746	–537.900	537.38	615.67	–53.3155
II	**566.72–784.73**	**19.452**	–	**40.28**	**|6133.3665|**	–	–	**|607.926|**
	566.72–695.34	13.529	651.38	46.22	1175.772	–	687.73	116.5399
	643.15–729	6.807	655.42	44.018	–475.431	661.97	720.51	–47.1237
	695.34–**784.73**	6.153	760.87	**40.28**	1574.903	–	777.32	156.1010
	729.15–883.15	7.088	799.64	36.795	–5276.621	750.70	829.90	–523.0073
III–IV	**784.73–1058.52**	**12.079**	**800.83**	**28.201**	**|28,301.855|**	–	–	**|2805.219|**
	784.73–950.46	7.425	800.83	32.848	9286.744	789.37	944.07	920.4821
	883.15–991.64	7.889	906.92	28.683	–5329.557	913.90	983.01	–528.2542
	950.46–**1058.52**	3.780	973.53	**28.201**	7400.922	958.42	1044.15	733.5635
	991.64–1196	0.514	1100.94	28.092	–7292.643	1001.77	1157.00	–722.8311
V	**1058.52–1223**	**0.142**	–	**28.059**	**|3646.3215|**	–	–	**|361.41555|**

Bold values denote important points which summarize and relate obtained results in each stage of the thermal decomposition of the gel precursors

changes, which are less defined in the range from about 450 K to 550 K of temperature. Finally, the last, fifth case is characterized by the biggest mass change, which is equal to 43.323%; however, the DSC curve has similar behaviour to those cases, which are shown in Fig. 2a, b.

As shown in Tables 2–6, stage II corresponds to the decomposition of metal tartrates. The mass of the gel precursors during this decomposition stage, in the range of temperature from 563 K to 803 K, decreases by 18.8–22.7%, except $Li_{0.05}Eu_{0.05}Ca_{0.9}MoO_4$ case, when the mass loss of about 20.2% ends at 837.5 K. The heat-treatment temperature of about 573 K is important because of the beginning of crystallization for the final $CaMoO_4$ double oxide. Furthermore, this endothermic process is competing with gradual decomposition of metal tartrates, which takes place until the partial stabilization of TG curve at about 873 K of temperature. By further increasing the heating temperature from 823 to 973 K, the mass change of the samples varies from 11.1 to 12.9% and is directly related to the burning of carbon-based residue, which is formed from the tartaric acid and metal tartrates at lower temperatures. Finally, the last mass change of the M−Eu–Ca−Mo–O tartrate gel precursors in the range of temperature from 1047 to 1223 K does not exceed 0.1%, and, except endothermic behaviour because of further growth of crystalline phases, no significant changes in the DSC curve were identified. Besides, it is important to note that in all cases, except for $Li_{0.05}Eu_{0.05}Ca_{0.9}MoO_4$ ceramic, the tendency of slight mass changes above 973 K was observed. The main reason of these changes is directly related to the partial releasing and evaporation of molybdenum oxide from the multicomponent oxide.

In order to show both the decomposition process of tartaric acid in the gel precursors and the overall mass change peculiarities of volatile components in the gels according to the gas atmosphere, the thermal analysis of as-prepared samples was also performed under inert flow. In this case, the TG/DTG/DSC measurements of the M–Eu–Ca−Mo–O tartrate (M=Li, Na, K, Rb, and Cs) gel precursors, which were carried out up to 1200 K at a heating rate of 20° min^{-1} in flowing nitrogen (20 cm^3 min^{-1}) at ambient pressure with a sample mass of about 5 mg, are shown in Fig. 3, respectively.

From these results, one is clear that the decomposition stages of tartaric acid only slightly depend according to the

Table 5 Thermoanalytical data of the Rb−Eu–Ca−Mo–O tartrate gel precursor for $Rb_{0.05}Eu_{0.05}Ca_{0.9}MoO_4$ ceramic

Stage No.	Range of temperature/K	Mass			Heat			
		Change/%	Onset/K	Residual/%	Flow/mJ	Onset/K	End/K	Enthalpy/J g^{-1}
I	**299.65–566.19**	**41.176**	–	**58.824**	**|968.5145|**	–	–	**|96.70655|**
	299.65–341.30	0.191	332.47	99.809	21.426	301.89	309.68	2.1394
	311.49–362.61	0.658	359.52	99.342	–76.810	318.40	356.71	–7.6695
	341.30–419.11	3.123	411.80	96.78	184.814	346.82	403.29	18.4537
	362.61–443.88	5.967	412.08	93.451	–89.368	392.30	437.43	–8.9234
	419.11–467.32	8.872	449.18	87.89	182.701	423.33	466.79	18.2428
	443.28–462.24	4.444	447.68	89.078	14.545	443.31	462.11	1.4524
	452.06–488.34	8.733	469.46	82.715	–14.978	455.42	–	–1.4955
	467.32–513.95	13.153	507.30	74.796	58.483	473.33	513.86	5.8396
	488.34–540.30	17.470	512.51	65.47	–44.617	507.34	–	–4.4550
	513.95–**566.19**	15.676	514.07	**58.824**	23.612	521.77	551.35	2.3577
	538.58–636	16.082	534.84	51.387	–514.321	537.12	602.70	–51.3551
II	**566.19–800.49**	**18.842**	–	**39.982**	**|4880.842|**	–	–	**|487.35315|**
	566.19–697.16	12.879	694.33	45.884	1415.820	573.47	693.07	141.3699
	648.68–737.53	6.915	691.67	43.312	–678.975	668.83	729.14	–67.7958
	697.16–**800.49**	5.841	701.52	**39.982**	847.161	708.83	779.09	84.5892
	708.83–883	7.419	722.70	37.712	–3363.451	751.14	847.33	–335.8414
III–IV	**800.49–1066.81**	**11.314**	–	**28.668**	**|29,664.8425|**	–	–	**|2962.04135|**
	800.49–949.68	7.338	943.04	32.567	7739.260	814.75	944.69	772.7669
	883–988.42	8.647	940.99	29.120	–6127.124	913.50	980.54	–611.7948
	949.68–**1066.81**	3.998	981.70	**28.668**	7613.912	957.72	1041.22	760.2508
	988.42–1219	0.524	1045.41	28.596	–13,005.642	995.33	1115.96	–1298.6163
V	**1066.81–1223**	**0.072**	–	**28.596**	**|6502.821|**	–	–	**|649.30815|**

Bold values denote important points which summarize and relate obtained results in each stage of the thermal decomposition of the gel precursors

heating atmosphere. The heating range in case of inert gas flow from 303 to 770 K (Fig. 3 left side) is almost identical compared with the cases presented in Fig. 2. Moreover, the behaviour of TG curves remains the same up to 873 K of temperature, and this concludes about similar heat-treatment effects, which are confirmed by DSC curves. Finally, the last mass change of the M–Eu–Ca–Mo–O tartrate gel precursors in the range of temperature from 873 to 950 K is attributed to the decomposition of a mixture from carbon and oxygen atoms, which are composed from the gel residue. This effect is confirmed by the results obtained from the K–Eu–Ca–Mo–O sample, where the behaviour of TG and DSC curves reiterates only in a more stretched range of temperature compared with the measurement in air flow.

In conclusion, it is also important to note that the total mass loss of all gel precursors well matches with the results obtained in an air atmosphere, while a prior mass change for the K–Eu–Ca–Mo–O sample above 873 K of temperature has no sufficient influence on the results, which were obtained in other heating conditions. Therefore, such an action is important only in the inert atmosphere and it is determined by the stability of final ceramics in a reducing environment. In this case, the combustion process in the air at temperatures above 873 K eliminates any specific conditions created by elemental carbon present in the sample.

FT-IR analysis

In order to show the characteristic group frequencies for the gel precursors in the mid-infrared region, the infrared spectroscopy (FT-IR) was performed. Corresponding FT-IR spectra are shown in Fig. 4, respectively.

According to the initial composition of the obtained M–Eu–Ca–Mo–O tartrate gel precursors, it is obvious that the stretching bands, which belong to the functional group frequencies of tartaric acid, in the infrared spectra are expected. It is well known that carboxylic acids (RCOOH) exist as dimers due to strong intermolecular hydrogen bonding. These compounds show a strong broad O–H stretching band in the 3300–2500 cm^{-1} range. The C=O stretching

band of the dimer is observed near 1700 cm^{-1}, while the free acid band is observed at higher wavenumbers (1760 cm^{-1}). In addition, carboxylic acids show characteristic C–O stretching and in-plane and out-of-plane O–H bending bands at 1240, 1430 and 930 cm^{-1}, respectively [38].

The range from 1660 to 1620 cm^{-1} is characteristic to the nitrate NO_2 asymmetric stretching. This band overlaps with the intensive stretching of the C=O group at 1700 cm^{-1} in the carboxylic acids. Moreover, the weak band of nitrate NO_2 symmetric stretching in the range from 1300 to 1270 am^{-1} is also observed. In addition, barely visible characteristic peak of nitrate N–O stretching in the range from 870 to 840 cm^{-1} was detected. Meanwhile, the characteristic stretching for the nitrate NO_2 bending (710–690 cm^{-1}) was not found [38]. Such a result explains the emergence of a peak in the DSC curve at 413.37 K, which tends to increase from the Li–Eu–Ca–Mo–O to Cs–Eu–Ca–Mo–O sample. This exothermal effect is closely related to the decomposition processes of the nitrate residue that left in the gel precursors after the evaporation procedure. The amount of corresponding nitrates in the gel precursors increases negligible and slightly influences the decomposition of the tartaric-acids dimer in the range of temperature from 416.55 to 455.48 K.

Fig. 3 Combined TG−DTG−DSC curves of the Li–Eu–Ca−Mo–O tartrate gel precursor for $Li_{0.05}Eu_{0.05}Ca_{0.9}MoO_4$ (**a**), $Na_{0.05}Eu_{0.05}Ca_{0.9}MoO_4$ (**b**), $K_{0.05}Eu_{0.05}Ca_{0.9}MoO_4$ (**c**), $Rb_{0.05}Eu_{0.05}Ca_{0.9}MoO_4$ (**d**) and $Cs_{0.05}Eu_{0.05}Ca_{0.9}MoO_4$ (**e**) ceramics. The overall view of the curves is shown on the right, and the highlighted temperature range from 303 to 770 K is presented on the left

The characteristic infrared bands of five-atom inorganic molecules, as well as for CrO_4^{2-} group, commonly are at the 890 cm^{-1} and 378 cm^{-1} of wavenumber. In all cases, the band at about 890 cm^{-1} observed in the FT-IR spectra, which is attributed to the vibrations of MoO_4^{2-} functional group [38]. Moreover, the vibrational frequencies of tetrahedral MoO_4^{2-}-type compound for their M–O vibrations are observed at 897 cm^{-1} (ν_1) and 837 cm^{-1} (ν_3), respectively [39]. Finally, the metal–oxygen characteristic vibrations similar to those observed in the crystalline Powellite structure of $CaMoO_4$ are attributed to the range from 800 to 500 cm^{-1} [40].

Table 6 Thermoanalytical data of the Cs−Eu–Ca−Mo–O tartrate gel precursor for $Cs_{0.05}Eu_{0.05}Ca_{0.9}MoO_4$ ceramic

Stage No.	Range of temperature/K	Mass			Heat			
		Change/%	Onset/K	Residual/%	Flow/mJ	Onset/K	End/K	Enthalpy/J g^{-1}
I	**299.79–561.54**	**43.323**	–	**56.677**	**|4359.4235|**	–	–	**|428.23425|**
	299.79–343.22	0.223	311.10	99.777	75.404	300.10	342.06	7.4071
	307.22–380.70	1.122	366.67	98.878	–47.110	333.49	361.68	–4.6277
	343.22–416.55	1.795	366.93	97.945	284.770	348.44	408.20	27.9735
	380.70–437.25	5.754	428.13	93.151	598.481	380.91	432.13	58.7899
	416.55–455.48	10.374	448.27	87.592	–720.661	420.79	449.57	–70.7919
	437.25–501.66	18.169	484.88	74.974	1301.827	440.10	501.07	127.8809
	455.48–**561.54**	30.676	486.13	**56.677**	326.086	455.71	533.85	32.0320
	487.08– 655.99	32.384	487.97	47.016	–2010.169	513.30	654.22	–197.4625
II	**561.54–800.77**	**18.833**	–	**37.844**	**|8610.0095|**	–	–	**|584.026|**
	561.54–704.83	13.810	688.15	42.964	2799.474	–	513.86	274.9975
	655.99–747.23	6.571	691.16	40.471	–1469.809	668.70	735.49	–144.3820
	704.83–**800.77**	5.409	710.50	**37.844**	1676.101	710.10	786.61	164.6465
	747.23–879.37	6.480	842.71	34.237	–3319.082	760.05	844.12	–326.0395
III–IV	**800.77–1007.27**	**11.152**	–	**26.692**	**|14,321.867|**	–	–	**|1406.86315|**
	800.77–958.45	9.360	936.22	28.315	6359.627	808.79	954.96	624.7178
	879.37–981.29	7.226	937.04	27.068	–3761.429	919.90	978.40	–369.4920
	985.45–**1007.27**	1.528	969.50	**26.692**	2027.409	963.81	1002.90	199.1561
	981.29–1042.75	0.185	983.51	26.721	–1027.722	986.96	1039.12	–100.9550
V	**1007.27–1220.77**	**0.169**	–	**26.523**	**|5297.426|**	–	–	**|520.376|**
	1007.27–1121.24	0.085	–	26.683	220.355	1028.07	1050.37	21.6459
	1042.75–1188.61	0.094	–	26.635	–4061.851	1045.16	1179.22	–399.0031
	1121.24–**1220.77**	0.090	–	**26.523**	501.359	1151.11	–	49.2495

Bold values denote important points which summarize and relate obtained results in each stage of the thermal decomposition of the gel precursors

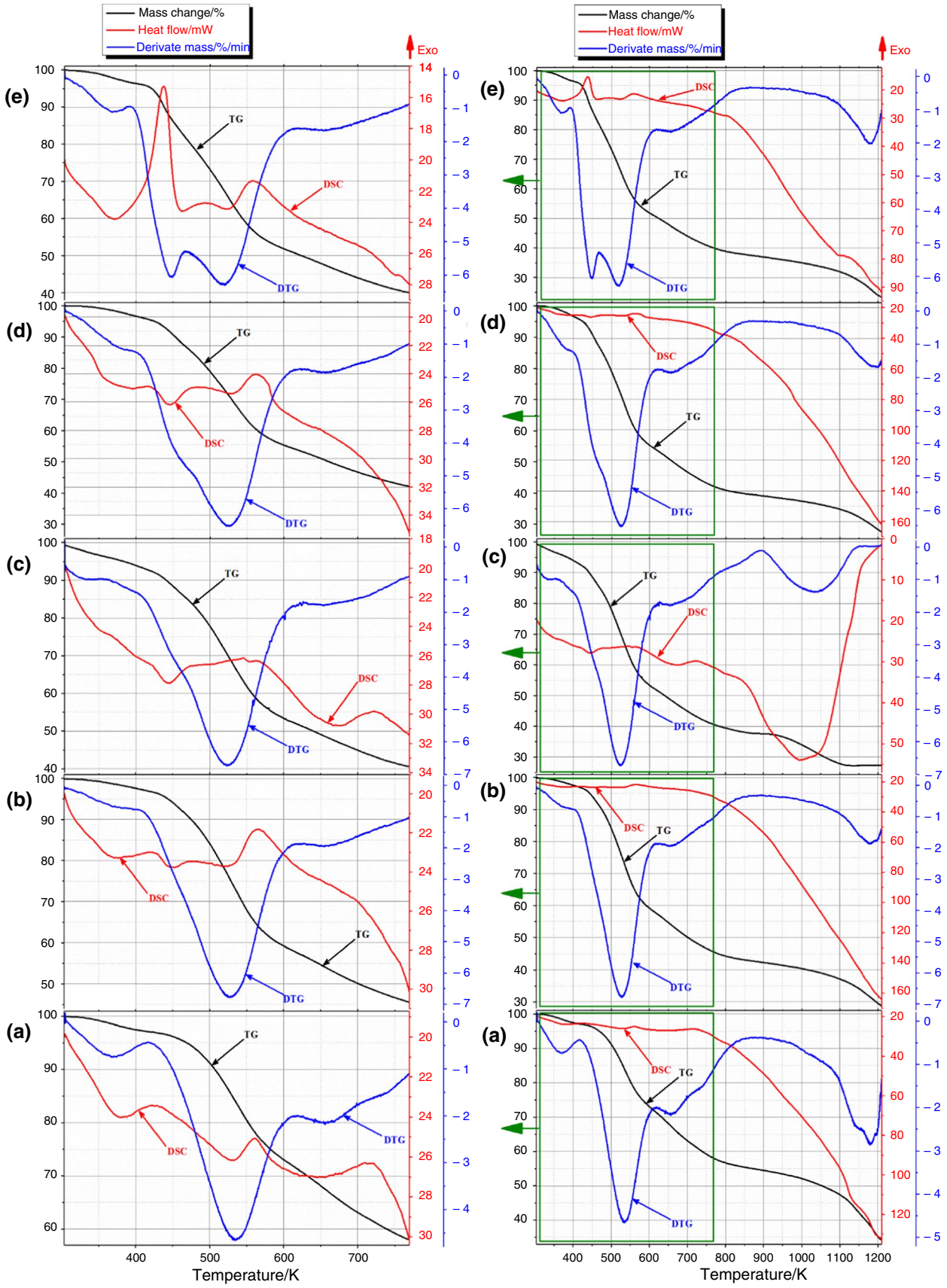
Mass change/%
Heat flow/mW
Derivate mass/%/min
Exo
(e)
(d)
(c)
(b)
(a)
TG
DSC
DTG
Temperature/K

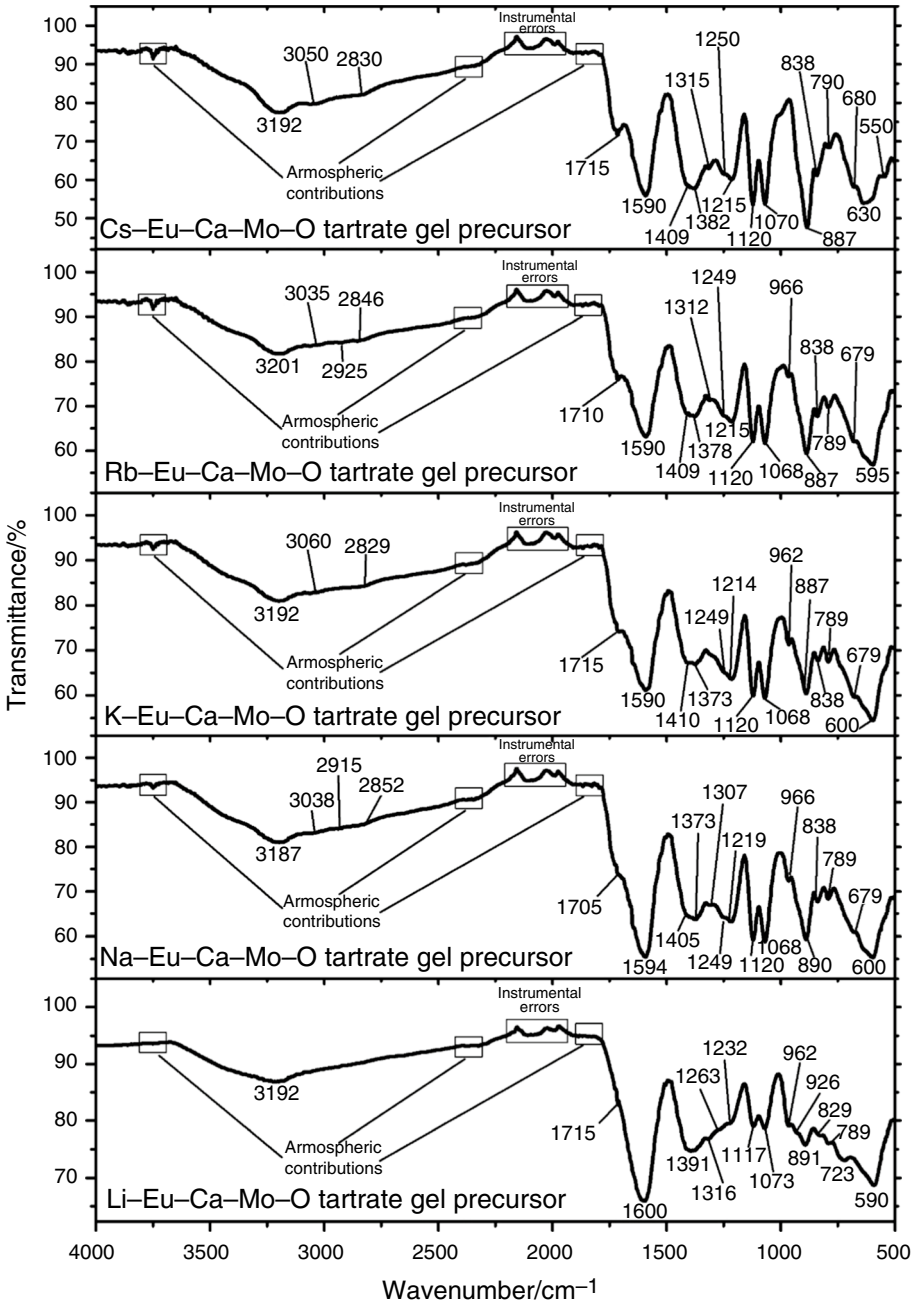

Fig. 4 FT-IR transmittance spectra of the M–Eu–Ca–Mo–O tartrate gel precursors dried at 393 K of temperature

X-ray diffraction

The powder x-ray diffraction (XRD) patterns of the Li–Eu–Ca−Mo–O tartrate gel precursor heat-treated at different temperatures shown in the top nine panels of Fig. 5 are well matched with the standard ICSD card of $CaMoO_4$ that is presented in the bottom panel.

No characteristic peaks attributable to the impurities by increasing heat-treatment temperature from 623 to 1273 K were identified. In addition, it is important to mention that drying of Li–Eu–Ca−Mo–O tartrate gel precursor for $Li_{0.05}Eu_{0.05}Ca_{0.9}MoO_4$ ceramic at 393 K showed fully amorphous character and no characteristic peaks to any crystalline compound from the XRD pattern were found. Besides, these results are in a good agreement with the TG−DTG−DSC data, when the crystallization of the final tetragonal phase below 623 K of temperature was estimated. Moreover, an important conclusion was made, by comparing these analysis

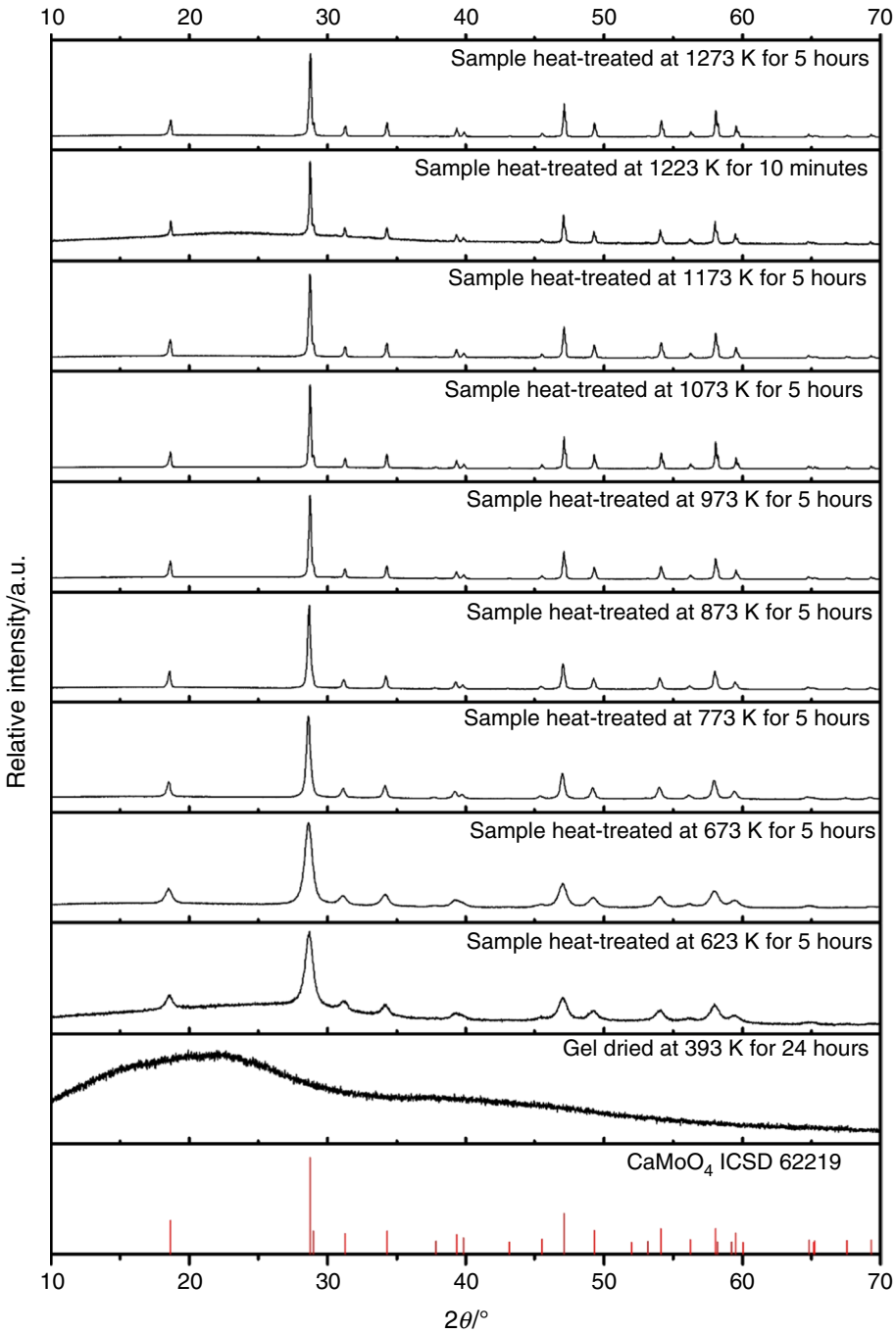

Fig. 5 Standard ICSD card of $CaMoO_4$ and XRD patterns of the Li–Eu–Ca−Mo–O tartrate gel precursor dried at 393 K for 24 h and heat-treated at temperatures of 623 K, 673 K, 773 K, 873 K, 973 K, 1073 K, 1173 K and 1273 K for 5 h in air

techniques that the crystallization of the final ceramic starts from about 568 K immediately after the initial decomposition of unreacted tartaric acid molecules into the elemental carbon and carbon oxides. According to above subject, the experimental and analysis results of other samples showed almost identical peculiarities. The end of the initial decomposition of tartaric acid for $Li_{0.05}Eu_{0.05}Ca_{0.9}MoO_4$, $Na_{0.05}Eu_{0.05}Ca_{0.9}MoO_4$, $K_{0.05}Eu_{0.05}Ca_{0.9}MoO_4$, $Rb_{0.05}Eu_{0.05}Ca_{0.9}MoO_4$ ceramics was similar and equal to 566 K of temperature, respectively. Meanwhile, the start of crystallization for $Cs_{0.05}Eu_{0.05}Ca_{0.9}MoO_4$ compound began at slightly lower 561 K of temperature. This effect was assigned to the increased ionic character of caesium, which plays a much more important role during the sol–gel formation stage, comparing it with other cases.

In order to prove that the crystallization of the final ceramics plays crucial role not only for the thermal decomposition of metal tartrates, but also strongly affects the

Table 7 Crystallite sizes, lattice parameter and density for the $M_{0.05}Eu_{0.05}Ca_{0.9}MoO_4$ (M=Li, Na, K, Rb, Cs) ceramics heat-treated at different temperatures for 5 and 0.15 h in air

Sample	Heat-treating temperature/K	Duration/h	Crystallite size/nm	Lattice parameter/pm		Density/g cm^{-3}
				a	c	
$Li_{0.05}Eu_{0.05}Ca_{0.9}MoO_4$	623	5	10.49	522.373	1143.005	4.26
$Na_{0.05}Eu_{0.05}Ca_{0.9}MoO_4$	623	5	10.83	522.397	1143.158	4.26
$K_{0.05}Eu_{0.05}Ca_{0.9}MoO_4$	623	5	8.20	522.358	1143.056	4.26
$Rb_{0.05}Eu_{0.05}Ca_{0.9}MoO_4$	623	5	8.30	522.270	1142.526	4.26
$Cs_{0.05}Eu_{0.05}Ca_{0.9}MoO_4$	623	5	8.98	522.427	1142.807	4.26
$Li_{0.05}Eu_{0.05}Ca_{0.9}MoO_4$	673	5	13.54	522.102	1142.770	4.26
$Na_{0.05}Eu_{0.05}Ca_{0.9}MoO_4$	673	5	13.17	522.202	1142.855	4.26
$K_{0.05}Eu_{0.05}Ca_{0.9}MoO_4$	673	5	11.29	522.307	1143.094	4.26
$Rb_{0.05}Eu_{0.05}Ca_{0.9}MoO_4$	673	5	11.37	522.298	1143.269	4.26
$Cs_{0.05}Eu_{0.05}Ca_{0.9}MoO_4$	673	5	13.89	522.285	1143.098	4.26
$Li_{0.05}Eu_{0.05}Ca_{0.9}MoO_4$	773	5	30.77	522.301	1142.666	4.26
$Na_{0.05}Eu_{0.05}Ca_{0.9}MoO_4$	773	5	26.78	522.471	1142.881	4.26
$Rb_{0.05}Eu_{0.05}Ca_{0.9}MoO_4$	773	5	25.61	522.429	1142.851	4.26
$Ca_{0.9}Rb_{0.05}Eu_{0.05}MoO_4$	773	5	22.61	522.540	1143.104	4.26
$Cs_{0.05}Eu_{0.05}Ca_{0.9}MoO_4$	773	5	20.48	522.509	1143.229	4.26
$Li_{0.05}Eu_{0.05}Ca_{0.9}MoO_4$	873	5	49.35	522.060	1142.922	4.26
$Na_{0.05}Eu_{0.05}Ca_{0.9}MoO_4$	873	5	42.79	522.101	1142.953	4.26
$K_{0.05}Eu_{0.05}Ca_{0.9}MoO_4$	873	5	39.58	522.462	1144.031	4.25
$Rb_{0.05}Eu_{0.05}Ca_{0.9}MoO_4$	873	5	41.06	522.452	1143.169	4.26
$Cs_{0.05}Eu_{0.05}Ca_{0.9}MoO_4$	873	5	47.10	522.227	1142.464	4.26
$Li_{0.05}Eu_{0.05}Ca_{0.9}MoO_4$	973	5	69.49	522.193	1142.434	4.26
$Na_{0.05}Eu_{0.05}Ca_{0.9}MoO_4$	973	5	62.38	522.292	1142.858	4.26
$K_{0.05}Eu_{0.05}Ca_{0.9}MoO_4$	973	5	69.92	522.776	1144.652	4.25
$Rb_{0.05}Eu_{0.05}Ca_{0.9}MoO_4$	973	5	72.52	522.545	1143.326	4.25
$Cs_{0.05}Eu_{0.05}Ca_{0.9}MoO_4$	973	5	53.48	522.464	1142.756	4.26
$Li_{0.05}Eu_{0.05}Ca_{0.9}MoO_4$	1073	5	96.87	522.215	1142.095	4.26
$Na_{0.05}Eu_{0.05}Ca_{0.9}MoO_4$	1073	5	78.51	522.498	1143.205	4.26
$K_{0.05}Eu_{0.05}Ca_{0.9}MoO_4$	1073	5	52.55	523.019	1145.099	4.24
$Rb_{0.05}Eu_{0.05}Ca_{0.9}MoO_4$	1073	5	54.78	522.707	1143.638	4.25
$Cs_{0.05}Eu_{0.05}Ca_{0.9}MoO_4$	1073	5	90.49	522.514	1142.921	4.26
$Li_{0.05}Eu_{0.05}Ca_{0.9}MoO_4$	1173	5	71.10	522.246	1142.217	4.26
$Na_{0.05}Eu_{0.05}Ca_{0.9}MoO_4$	1173	5	81.91	522.492	1143.019	4.26
$K_{0.05}Eu_{0.05}Ca_{0.9}MoO_4$	1173	5	78.28	522.749	1143.999	4.25
$Rb_{0.05}Eu_{0.05}Ca_{0.9}MoO_4$	1173	5	135.13	522.668	1143.655	4.25
$Cs_{0.05}Eu_{0.05}Ca_{0.9}MoO_4$	1173	5	84.42	522.481	1142.981	4.26
$Li_{0.05}Eu_{0.05}Ca_{0.9}MoO_4$	1223	0.15	110.36	522.939	1144.544	4.24
$Na_{0.05}Eu_{0.05}Ca_{0.9}MoO_4$	1223	0.15	336.88	523.020	1144.328	4.24
$K_{0.05}Eu_{0.05}Ca_{0.9}MoO_4$	1223	0.15	141.21	523.385	1145.669	4.23
$Rb_{0.05}Eu_{0.05}Ca_{0.9}MoO_4$	1223	0.15	190.14	523.227	1145.105	4.24
$Cs_{0.05}Eu_{0.05}Ca_{0.9}MoO_4$	1223	0.15	105.76	523.113	1144.228	4.24
$Li_{0.05}Eu_{0.05}Ca_{0.9}MoO_4$	1273	5	85.81	522.351	1142.570	4.26
$Na_{0.05}Eu_{0.05}Ca_{0.9}MoO_4$	1273	5	146.74	522.586	1143.192	4.25
$K_{0.05}Eu_{0.05}Ca_{0.9}MoO_4$	1273	5	57.37	522.564	1143.153	4.26
$Rb_{0.05}Eu_{0.05}Ca_{0.9}MoO_4$	1273	5	53.45	522.482	1142.924	4.26
$Cs_{0.05}Eu_{0.05}Ca_{0.9}MoO_4$	1273	5	76.37	522.497	1142.939	4.26

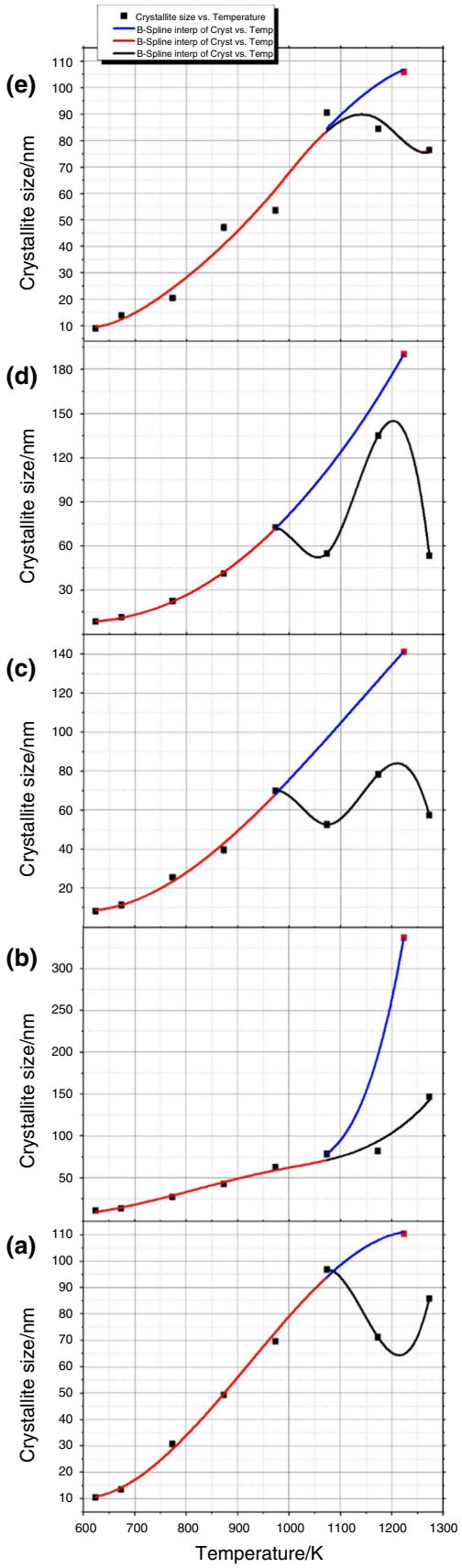

Fig. 6 Plot of crystallite size versus heat-treatment temperature for $Li_{0.05}Eu_{0.05}Ca_{0.9}MoO_4$ (**a**), $Na_{0.05}Eu_{0.05}Ca_{0.9}MoO_4$ (**b**), $K_{0.05}Eu_{0.05}Ca_{0.9}MoO_4$ (**c**), $Rb_{0.05}Eu_{0.05}Ca_{0.9}MoO_4$ (**d**) and $Cs_{0.05}Eu_{0.05}Ca_{0.9}MoO_4$ (**e**) ceramics

physical properties, the Rietveld refinement analysis of XRD patterns for the synthesized multicomponent oxides was applied. The crystallite sizes and lattice parameter for the $Li_{0.05}Eu_{0.05}Ca_{0.9}MoO_4$, $Na_{0.05}Eu_{0.05}Ca_{0.9}MoO_4$, $K_{0.05}Eu_{0.05}Ca_{0.9}MoO_4$, $Rb_{0.05}Eu_{0.05}Ca_{0.9}MoO_4$, and $Cs_{0.05}Eu_{0.05}Ca_{0.9}MoO_4$ compounds heat-treated at different temperatures are shown in Table 7.

The dependency of the crystallite size versus temperature, collected from the Table 7, is shown in Fig. 6, respectively.

From these curve graphs, it is clear that by increasing the sintering for $M_{0.05}Eu_{0.05}Ca_{0.9}MoO_4$ ceramics from 623 to 973 K, the values of crystallite size tend to increase; however, at somewhat higher temperatures their decreasing trends were observed. It is important to take attention to the fact that for $Li_{0.05}Eu_{0.05}Ca_{0.9}MoO_4$, $Na_{0.05}Eu_{0.05}Ca_{0.9}MoO_4$ and $Cs_{0.05}Eu_{0.05}Ca_{0.9}MoO_4$ ceramics, the decrease in the size for crystallites starts only above 1073 K of temperature. Meanwhile, the crystallites for $K_{0.05}Eu_{0.05}Ca_{0.9}MoO_4$ and $Rb_{0.05}Eu_{0.05}Ca_{0.9}MoO_4$ ceramics start to decrease already above 973 K. This effect is directly related to the crystallization of europium oxide [41], besides, depending on the nature of alkali metal in the ceramic, the growth of crystallites takes place at a different temperature.

SEM micrographs

According to such quite unexpected results obtained from the Rietveld refinement of XRD patterns, the surface morphology of $K_{0.05}Eu_{0.05}Ca_{0.9}MoO_4$ and $Rb_{0.05}Eu_{0.05}Ca_{0.9}MoO_4$ samples sintered at 1073 K for 5 h in air was also investigated. Corresponding SEM micrographs of these ceramics are shown in Fig. 7.

As shown in Fig. 7a, the surface of the K–Eu–Ca−Mo–O tartrate gel precursor for $K_{0.05}Eu_{0.05}Ca_{0.9}MoO_4$ ceramic heat-treated at 1073 K consists of spherical-like aggregated particles, which size varies from 200 nm to 1.2 µm. Meanwhile, the surface morphology of the Rb–Eu–Ca−Mo–O tartrate gel precursor for $Rb_{0.05}Eu_{0.05}Ca_{0.9}MoO_4$ ceramic (Fig. 7b) consists of similar particles to those observed from the case shown in Fig. 7a, which sizes varies from 200 nm to 1.8 µm, respectively. In conclusion, it is clear that surface of both samples is almost identical and the difference that comes into existence is only related to the degree of either agglomeration or aggregation of individual particles.

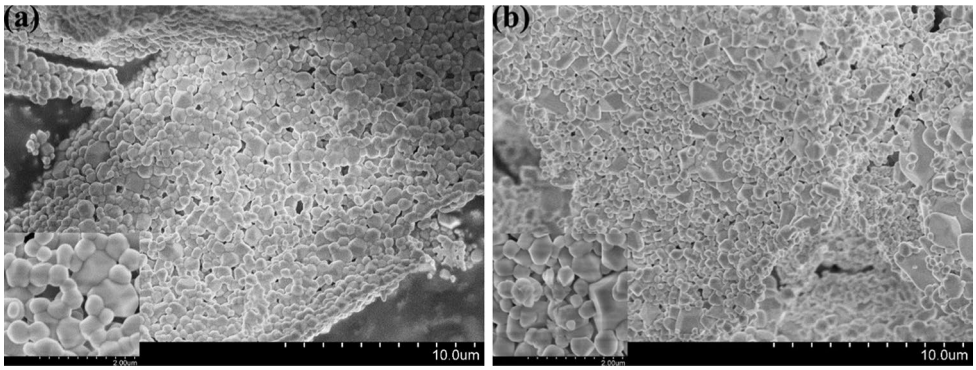

Fig. 7 SEM micrographs of M–Eu–Ca−Mo–O tartrate gel precursors for $K_{0.05}Eu_{0.05}Ca_{0.9}MoO_4$ (**a**) and $Rb_{0.05}Eu_{0.05}Ca_{0.9}MoO_4$ (**b**) ceramics heat-treated at 1073 K temperatures

PL analysis

In order to show the relation between the growth mechanism of the crystallites and luminescence properties of the ceramics prepared at 773 K of temperature, the photoluminescence (PL) measurement were applied. Corresponding PL excitation spectra of the $M_{0,05}Eu_{0,05}Ca_{0,9}MoO_4$ (where M=Li, Na, K, Rb, Cs) ceramics are shown in Fig. 8. The characteristic bands were registered with a fixed excitation at 395 nm of wavelength with emerged transitions from $^7F_0 \rightarrow {}^5L_6$ to $^7F_0 \rightarrow {}^5D_2$. This result matches well with UVLED and blue LED, respectively [42].

The PLE spectra (Fig. 9) show characteristic $^5D_0 \rightarrow {}^7F_J$ (J = 0, 1, 2, 3, 4) Eu^{3+} emission lines, which are summed up in Table 8 [43].

From the data displayed in the Table 8, it is clear that $^5D_0 \rightarrow {}^7F_3$ transition is forbidden, which is observed only in $Na_{0,05}Eu_{0,05}Ca_{0,9}MoO_4$, $Cs_{0,05}Eu_{0,05}Ca_{0,9}MoO_4$, $Rb_{0,05}Eu_{0,05}Ca_{0,9}MoO_4$ samples, and such phenomena are explained only as J—mixing [43]. The characteristic emissions of Eu^{3+} from $^5D_1$ are less common case; however, the peaks of $^5D_1 \rightarrow {}^7F_2$ and $^5D_1 \rightarrow {}^7F_1$ transitions were observed, which intensities are comparable with $^5D_0 \rightarrow {}^7F_1$ characteristic emission. Meanwhile, the $^5D_0 \rightarrow {}^7F_0$ transition is strictly forbidden according to the standard Judd–Ofelt theory; however, as was mentioned before, it could be explained by assuming that this transition is due to J—mixing [43]. Moreover, this transition is also an indicator of C_{nv}, C_n or C_s symmetries, because other symmetries do not produce observable spectral line. According to the results obtained in this work, a comparative study of the substitution effect on the intensity of luminescence by comparing intensity of $^5D_0 \rightarrow {}^7F_2$ transition was also performed. Despite the fact that this transition of 4f configuration is hypersensitive to the symmetry and crystal field of Eu^{3+} ion, the ratio R of intensities for $^5D_0 \rightarrow {}^7F_2$ and $^5D_0 \rightarrow {}^7F_1$ characteristic emissions was used instead and expressed as $I(^5D_0 \rightarrow {}^7F_2)/I(^5D_4 \rightarrow {}^7F_1)$, respectively. Figure 10 shows the before-mentioned ratio R distribution and its dependency from the crystallite size for $M_{0,05}Eu_{0,05}Ca_{0,9}MoO_4$ ceramics.

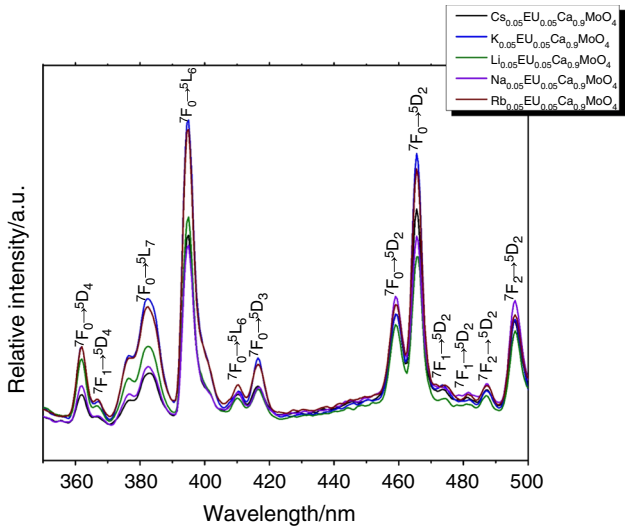

Fig. 8 PL ($\lambda_{ex} = 395$ nm) spectra of M–Eu–Ca−Mo–O tartrate (M=Li, Na, K, Rb and Cs) gel precursors for $M_{0.05}Eu_{0.05}Ca_{0.9}MoO_4$ ceramics heat-treated at 773 K

From Fig. 10, it is clear that either growing or decreasing correlation cannot be observed. However, these results showed an interesting trend, which is directly related to both the sizes of crystallite that grew up at 773 K and the formation mechanism of obtained crystals at higher heat-treating temperatures. It is well known that smaller crystallites produce higher luminescence intensity. This is due to the fact that smaller crystallites would have less surface imperfections quenching luminescence and less energy would be wasted in bulk material as heat dissipation. On the other hand, this study also proved that further growth of crystallites at much higher temperatures completely differs according to the nature of alkali metal. This effect mainly depends from the distribution of metal salts in the gel, which formation, during the sol–gel processing, was influenced by interaction of individual ion. By the way, such conclusion shows that the optical properties of prepared ceramics are strongly affected by several factors, and the correlation is not always expected. Moreover, the tendencies of differences of

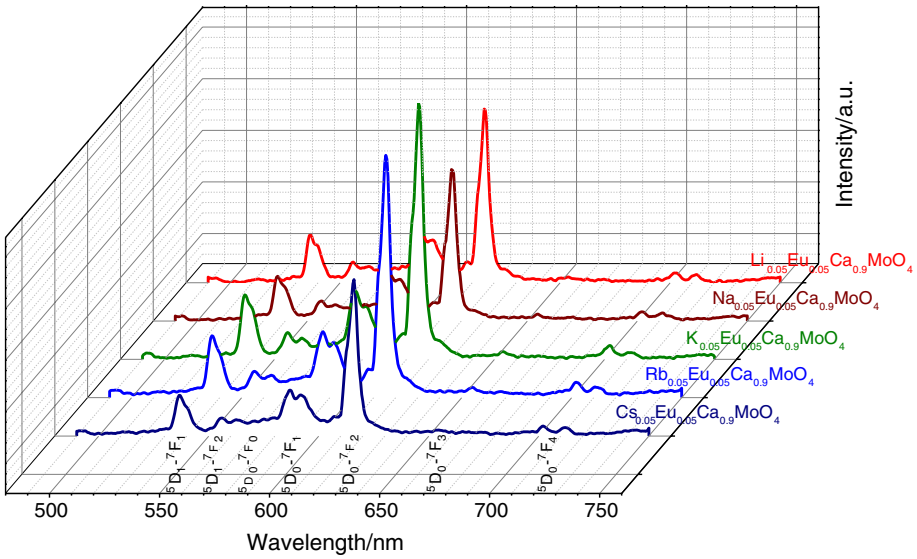

Fig. 9 PLE (λ_{em} = 616 nm) spectra of M–Eu–Ca−Mo–O tartrate (M=Li, Na, K, Rb and Cs) gel precursors for $M_{0.05}Eu_{0.05}Ca_{0.9}MoO_4$ ceramics heat-treated at 773 K

Table 8 Overview of the transitions observed in luminescence spectra of europium (III) compounds [43]

Transition	Dipole character	Wavelength	Remarks
$^5D_0 \rightarrow {}^7F_0$	ED	570–585	Only observed in C_n, C_{nv} and C_s symmetry
$^5D_0 \rightarrow {}^7F_1$	MD	585–600	Intensity largely independent of environment
$^5D_0 \rightarrow {}^7F_2$	ED	610–630	Hypersensitive transition; intensity very strongly dependent on environment
$^5D_0 \rightarrow {}^7F_3$	ED	640–660	Forbidden transition
$^5D_0 \rightarrow {}^7F_4$	ED	680–710	Intensity dependent on environment, but no hypersensitivity

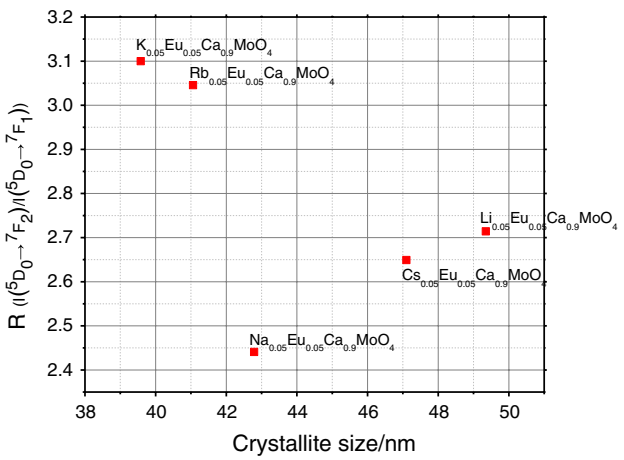

Fig. 10 Plot of R versus crystallite size for $M_{0.05}Eu_{0.05}Ca_{0.9}MoO_4$ ceramics

both the physical properties and structural features for each ceramic sample remain even by increasing the heat-treating temperature.

Conclusions

Summarizing the results obtained from the TG/DTG/DSC, XRD, SEM and PL measurements, it can be concluded that the tartaric acid-assisted synthesis of M–Eu–Ca−Mo–O tartrate (M=Li, Na, K, Rb, and Cs) gel precursors for nano-sized $M_{0.05}Eu_{0.05}Ca_{0.9}MoO_4$ ceramics is suitable preparation technique, which enables the detail investigation of multicomponent metal oxides in the frame of their chemical and physical properties. According to the thermal analysis, the decomposition of metal–tartrate gel precursors occurs in similar manner. Meanwhile, the emerging differences that mainly focus on the thermal decomposition of unreacted tartaric acid molecules, which mechanism depends on the coordination ability of the corresponding alkali metal. Besides, in all cases, except for $Li_{0.05}Eu_{0.05}Ca_{0.9}MoO_4$ ceramic, the tendency of slight mass changes above 973 K was observed. The FT-IR spectra of the M–Eu–Ca–Mo–O tartrate gels revealed that a small number of nitrates were left in the precursors. The XRD patterns correlated with the results of thermal analysis perfectly do not indicate any

characteristic peaks attributable to the impurities by increasing the heat-treatment temperature from 623 to 1273 K. The dependency of the crystallite size versus temperature clearly showed that by increasing the heat-treating temperature from 623 to 973 K for $M_{0.05}Eu_{0.05}Ca_{0.9}MoO_4$ ceramics, the values of crystallite size tend to increase; however, at higher temperatures the decreasing trends of crystallites were observed. The reason of this behaviour directly depends from the start of the crystallization of europium (III) oxide. The study of surface morphology indicated the almost identical trends of morphological properties for the analyzed samples with the spherical particles, which size varies from 200 nm to 1.5 μm. The results of the PL studies revealed that the crystallite size and the mechanism of their growing tendencies for the $M_{0.05}Eu_{0.05}Ca_{0.9}MoO_4$ compounds are closely related to the ratio R of intensities for $^5D_0 \rightarrow {}^7F_2$ and $^5D_0 \rightarrow {}^7F_1$ characteristic emissions. Finally, it was concluded that the nature of alkali metal strongly affects the distribution of Eu_2O_3 in the $CaMoO_4$ host and the reasons of such behaviour are basically determined by the different chemical activity of alkali metals in the range of temperature from 623 to 1073 K.

Acknowledgements This research was funded by the European Social Fund under the No 09.3.3-LMTK-712 "Development of Competences of Scientists, other Researchers and Students through Practical Research Activities" measure.

References

1. Hou ZY, Chai RT, Zhang ML, Zhang CM, Chong P, Xu ZH, et al. Fabrication and luminescence properties of one-dimensional CaMoO4:Ln^{3+} (Ln=Eu, Tb, Dy) Nanofibers via Electrospinning Process. Langmuir. 2009;25(20):12340–8.
2. Gao DJ, Lai X, Cui CH, Cheng P, Bi J, Lin DM. Oxidant-assisted preparation of $CaMoO_4$ thin film using an irreversible galvanic cell method. Thin Solid Films. 2010;518(12):3151–5.
3. Lei F, Yan B. Hydrothermal synthesis and luminescence of CaMO4:RE^{3+} (M=W, Mo; RE=Eu, Tb) submicro-phosphors. J Solid State Chem. 2008;181(4):855–62.
4. Thongtem T, Kungwankunakorn S, Kuntalue B, Phuruangrat A, Thongtem S. Luminescence and absorbance of highly crystalline $CaMoO_4$, $SrMoO_4$, $CaWO_4$ and $SrWO_4$ nanoparticles synthesized by co-precipitation method at room temperature. J Alloy Compd. 2010;506(1):475–81.
5. Hosseinpour-Mashkani SS, Hosseinpour-Mashkani SS, Sobhani-Nasab A. Synthesis and characterization of rod-like CaMoO4 nanostructure via free surfactant sonochemical route and its photocatalytic application. J Mater Sci Mater Electron. 2016;27(5):4351–5.
6. Silva MMS, Sena MS, Lopes-Moriyama AL, Souza CP, Santos AG. Experimental planning of the synthesis of strontium molybdate by EDTA-citrate and its structural influence, morphology and optical bandgap. Ceram Int. 2018;44(14):16606–14.
7. Sun Y, Ma JF, Jiang XH, Fang JR, Song ZW, Gao C, et al. Ethylene glycol-assisted electrochemical synthesis of $CaMoO_4$ crystallites with different morphology and their luminescent properties. Solid State Sci. 2010;12(7):1283–6.
8. Parchur AK, Ningthoujam RS, Rai SB, Okram GS, Singh RA, Tyagi M, et al. Luminescence properties of Eu^{3+} doped $CaMoO_4$ nanoparticles. Dalton Trans. 2011;40(29):7595–601.
9. Wang YG, Ma JF, Tao JT, Zhu XY, Zhou J, Zhao ZQ, et al. Low temperature synthesis of $CaMoO_4$ nanoparticles. Ceram Int. 2007;33(4):693–5.
10. Raju GSR, Pavitra E, Ko YH, Yu JS. A facile and efficient strategy for the preparation of stable $CaMoO_4$ spherulites using ammonium molybdate as a molybdenum source and their excitation induced tunable luminescent properties for optical applications. J Mater Chem. 2012;22(31):15562–9.
11. Li X, Yang ZP, Guan L, Guo JX, Wang Y, Guo QL. Synthesis and luminescent properties of $CaMoO_4$:Tb^{3+}, R + (Li + , Na + , K +). J Alloy Compd. 2009;478(1–2):684–6.
12. Zhang ZJ, Chen HH, Yang XX, Zhao JT. Preparation and luminescent properties of Eu^{3+} and Tb^{3+} ions in the host of $CaMoO_4$. Mater Sci Eng B Solid State Mater Adv Technol. 2007;145(1–3):34–40.
13. Luo YS, Dai XJ, Zhang WD, Yang Y, Sun CQ, Fu SY. Controllable synthesis and luminescent properties of novel erythrocyte-like $CaMoO_4$ hierarchical nanostructures via a simple surfactant-free hydrothermal route. Dalton Trans. 2010;39(9):2226–31.
14. Marques VS, Cavalcante LS, Sczancoski JC, Alcantara AFP, Orlandi MO, Moraes E, et al. Effect of different solvent ratios (water/ethylene glycol) on the growth process of $CaMoO_4$ crystals and their optical properties. Cryst Growth Des. 2010;10(11):4752–68.
15. Parchur AK, Ningthoujam RS. Preparation and structure refinement of Eu^{3+} doped $CaMoO_4$ nanoparticles. Dalton Trans. 2011;40(29):7590–4.
16. Dutta S, Som S, Sharma SK. Luminescence and photometric characterization of $^{K+}$ compensated $CaMoO_4$:Dy^{3+} nanophosphors. Dalton Trans. 2013;42(26):9654–61.
17. Haque MM, Kim DK. Luminescent properties of Eu^{3+} activated MLa2(MoO4)(4) based (M=Ba, Sr and Ca) novel red-emitting phosphors. Mater Lett. 2009;63(9–10):793–6.
18. Cavalli E, Boutinaud P, Mahiou R, Bettinelli M, Dorenbos P. Luminescence dynamics in Tb^{3+}-doped $CaWO_4$ and $CaMoO_4$ crystals. Inorg Chem. 2010;49(11):4916–21.
19. Parchur AK, Prasad AI, Ansari AA, Rai SB, Ningthoujam RS. Luminescence properties of Tb^{3+}-doped $CaMoO_4$ nanoparticles: annealing effect, polar medium dispersible, polymer film and core-shell formation. Dalton Trans. 2012;41(36):11032–45.
20. Zhang JH, Wang L, Jin Y, Zhang X, Hao ZD, Wang XJ. Energy transfer in $Y_3Al_5O_{12}$:Ce^{3+}, Pr^{3+} and $CaMoO_4$:Sm^{3+}, Eu^{3+} phosphors. J Lumin. 2011;131(3):429–32.
21. Liu XG, Li L, Noh HM, Jeong JH, Jang K, Shin DS. Controllable synthesis of uniform $CaMoO_4$:Eu^{3+}, M^+(M=Li, Na, K) microspheres and optimum luminescence properties. RSC Adv. 2015;5(13):9441–54.
22. Laguna M, Nunez NO, Becerro AI, Ocana M. Morphology control of uniform $CaMoO_4$ microarchitectures and development of white light emitting phosphors by Ln doping (Ln=Dy^{3+}, Eu^{3+}). CrystEngComm. 2017;19(12):1590–600.
23. Cho K, Choi J, Kim KM, Kim TW, Lee JI, Ryu JH. Pulsed laser synthesis of Er^{3+}/Yb^{3+}Co-doped $CaMoO_4$ colloidal nanocrystal and its upconversion luminescence. J Nanosci Nanotechnol. 2016;16(6):6344–9.
24. Choi GK, Kim JR, Yoon SH, Hong KS. Microwave dielectric properties of scheelite (A=Ca, Sr, Ba) and wolframite (A=Mg, Zn, Mn) AMoO(4) compounds. J Eur Ceram Soc. 2007;27(8–9):3063–7.
25. Yan SX, Zhang JH, Zhang X, Lu SZ, Ren XG, Nie ZG, et al. Enhanced red emission in $CaMoO_4$:Bi^{3+}, Eu^{3+}. J Phys Chem C. 2007;111(35):13256–60.

26. Parhi P, Singh SS, Ray AR, Ramanan A. Mechanochemically assisted room temperature solid state metathesis reaction for the synthesis of $MMoO_4$ (M=Ca, Sr and Ba). Bull Mat Sci. 2006;29(2):115–8.
27. Yu S, Lin ZB, Zhang LZ, Wang GF. Preparation of monodispersed Eu^{3+}:$CaMoO_4$ nanocrystals with single quasihexagon. Cryst Growth Des. 2007;7(12):2397–9.
28. Yoon JW, Ryu JH, Shim KB. Photoluminescence in nanocrystalline MMoO4 (M=Ca, Ba) synthesized by a polymerized complex method. Mater Sci Eng B Solid State Mater Adv Technol. 2006;127(2–3):154–8.
29. Wangkhem R, Yaba T, Singh NS, Ningthoujam RS. Red emission enhancement from $CaMoO_4$:Eu^{3+} by co-doping of Bi^{3+} for near UV/blue LED pumped white pcLEDs: energy transfer studies near. J Appl Phys. 2018;123(12):10.
30. Yin YK, Gao Y, Sun YZ, Zhou BB, Ma L, Wu X, et al. Synthesis and photoluminescent properties of $CaMoO_4$ nanostructures at room temperature. Mater Lett. 2010;64(5):602–4.
31. Shi S, Gao J, Zhou J. Effects of charge compensation on the luminescence behavior of Eu^{3+} activated $CaWO_4$ phosphor. Opt Mater. 2008;30(10):1616–20.
32. Kim KM, Ryu JH, Mhin SW, Park GS, Shim KB. Luminescence of nanocrystalline Tb(3)Al(5)O(12): Ce(3+) phosphors synthesized by nitrate-citrate gel combustion method. J Electrochem Soc. 2008;155(10):J293–6.
33. Lian JB, Qin H, Liang P, Liu F. Co-precipitation synthesis of $Y_2O_2SO_4$:Eu^{3+} nanophosphor and comparison of photoluminescence properties with Y_2O_2:Eu^{3+} and Y_2O_2S:Eu^{3+} nanophosphors. Solid State Sci. 2015;48:147–54.
34. Cho H, Hwang SM, Bin Lee J, Ka DH, Kim TW, Lee BS, et al. White luminescence of Ho^{3+}/Tm^{3+}/Yb^{3+}-codoped $CaWO_4$ synthesized via citrate complex route assisted by microwave irradiation. Trans Nonferrous Met Soc China. 2014;24:S134–40.
35. Braziulis G, Janulevicius G, Stankeviciute R, Zalga A. Aqueous sol-gel synthesis and thermoanalytical study of the alkaline earth molybdate precursors. J Therm Anal Calorim. 2014;118(2):613–21.
36. Braziulis G, Stankeviciute R, Zalga A. Sol–gel derived europium doped $CaMoO_4$:Eu^{3+} with complex microstructural and optical properties. Mater Sci Medzg. 2014;20(1):90–6.
37. Zalga A, Gaidamaviciene GE, Gricius Z, Uzpurvyte E, Gadeikis J, Diktanaite A, et al. Aqueous sol-gel synthesis, thermoanalytical study and electrical properties of $La_2Mo_2O_9$. J Therm Anal Calorim. 2018;132(3):1499–511.
38. Stuart B. Infrared spectroscopy: fundamentals and applications. West Sussex: Wiley; 2004.
39. Nakamoto K. Infrared and Raman Spectra of Inorganic and Coordination Compounds. Handbook of Vibrational Spectroscopy. 2006.
40. Braziulis G, Stankeviciute R, Zalga A. Sol-gel derived europium doped $CaMoO_4$:Eu^{3+} with complex microstructural and optical properties. Mater Sci. 2014;20(1):90–6.
41. Curtis C, Tharp A. Ceramic properties of europium oxide. J Am Ceram Soc. 1959;42(3):151–6.
42. Liu J, Lian HZ, Shi CS. Improved optical photoluminescence by charge compensation in the phosphor system $CaMoO_4$:Eu^{3+}. Opt Mater. 2007;29(12):1591–4.
43. Binnemans K. Interpretation of europium(III) spectra. Coord Chem Rev. 2015;295:1–45.